Eur. Phys. J. Plus (2023) 138:511
https://doi.org/10.1140/epjp/s13360-023-04133-8

THE EUROPEAN PHYSICAL JOURNAL PLUS

Regular Article

Bottom side partially etched D-shaped PCF biosensor for early diagnosis of cancer cells

Shivam Singh[1], **Bhargavi Chaudhary**[2], **Anurag Upadhyay**[3,a], **Sofyan A. Taya**[4,b]

[1] Department of Electronics and Communication Engineering, ABES Engineering College, Ghaziabad, Uttar Pradesh, India
[2] Department of Electrical Engineering, Indian Institute of Technology Delhi, New Delhi, India
[3] Department of Applied Science and Humanities, Rajkiya Engineering College, Uttar Pradesh, Azamgarh, India
[4] Physics Department, Islamic University of Gaza, P.O. Box 108, Gaza, Palestine

Received: 29 October 2022 / Accepted: 23 May 2023

Abstract In this work, we developed a dual-side polished solid core (single transmission channel) photonic crystal fiber (PCF) sensor that can efficiently detect cancer cells in the blood, adrenal gland, cervical, breast, and skin tissues, among other body parts. The concept of surface plasmon resonance has been exploited to conceive the functionality of our proposed PCF cancer sensor, and gold (Au) is used as an active metal to provide the plasmonic effect. The bottom portion of PCF has been partially etched and is coated with gold. Moreover, to uplift the plasmonic oscillations near the gold-PCF interface, its thickness (t_{Au}) has been optimized to 40 nm. In our investigation, we have considered the liquid forms of both healthy and cancer-affected samples pertaining to their refractive indices. This is because it is easy to inject liquid samples into the sensing channel using capillaries or suction pumps. The cancer-affected liquid sample to be tested produces a distinct absorption peak in the form of a resonance wavelength when applied to the sensing area (gold-coated fiber), which is different from the absorption peak of the healthy sample. Sensitivity is measured using this shuffling of the absorption peak. Therefore, the wavelength sensitivities extracted from the proposed cancer sensor for adrenal gland cancer cells, blood cancer cells, breast cancer cells, cervical cancer cells, and skin cancer cells are 17,857.14 nm/RIU, 23,214.28 nm/RIU, 19,285.71 nm/RIU, 22,857.14 nm/RIU, 17,916.66 nm/RIU and 18,000 nm/RIU, respectively, including maximum detection limit 0.024. These numerical outcomes of our proposed cancer sensor prove its great credibility in cancer cell detection.

1 Introduction

Photonic crystal fiber (PCF) is a revolutionary form of fiber structure that emerged to get over the constraints of classical fiber, which include significant propagation loss, poor dispersion control, and low power handling capacity [1]. PCF has got the advantage of minimal propagation losses over conventional fiber due to microstructured pores running along the fiber length. Moreover, the other useful advantages are high birefringence, large nonlinearity, endless single-mode operation, and negative/zero dispersion [2, 3]. Until now, numerous improvements to fiber structures have been made to match state-of-the-art optical fiber technologies for various real-world applications [4, 5]. Microstructure PCF has revolutionized the field of optical sensing because of its potential uses in a wide variety of sensing applications, such as magnetic field sensing, temperature sensing, strain sensing, and hydro pressure sensing [6–9]. Additionally, PCF has shown its effectiveness in glucose sensing, water salinity sensing, and pH sensing [10–13]. In the past few decades, biosensing has been escalated at a faster rate due to its significant applications in food quality control and health monitoring. The major benefit of biosensors is their natural sensitivity and selectivity. In recent years, optical biosensing has gained popularity. When any analyte or molecule is detected using optical biosensors, there is a knock-on effect that causes light to be either absorbed or emitted. Optical biosensors use a variety of biosensing methods, including surface plasmon resonance (SPR), luminescence, and absorption. Among them, SPR is a method that is frequently utilized for biosensing applications [14]. In PCF-based SPR biosensors, incoming light partially penetrates the cladding in the form of evanescent wave and interacts with the plasmonic material (active metal) as it travels through the fiber core. The free electrons on the metallic surface are stimulated by these interactions. When the frequency of this evanescent wave coincides with that of the oscillating free surface electrons of the plasmonic material, resonance of the free electrons occurs, leading to the creation of surface plasmon waves (SPWs). A narrow band peak of propagation loss is produced under resonance condition. This resonance peak reallocates when the analyte/sample refractive index changes near the metal surface. These days, PCFs are being employed in optical biosensing with the purpose of

[a] e-mail: anurag.upadhyay009@gmail.com (corresponding author)
[b] e-mail: staya@iugaza.edu.ps (corresponding author)

Published online: 08 June 2023

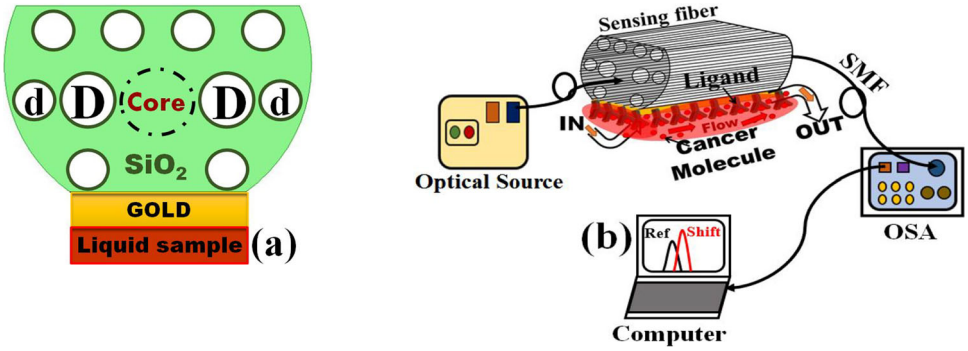

Fig. 1 **a** 2D front cross section and **b** experimental set-up of the designed biosensor

identifying and preventing dangerous disorders that could endanger human life Cancer is considered a fatal pandemic disease in the world, as it caused nearly 22.54 lakh deaths in India in the year 2018–2020. Cancer is a wider domain of diseases, and nearly 100 diseases are under its domain. Cancer is the unusual and uncontrolled growth of cells that leads to the formation of tumors, and it can spread to other tissues. Physical carcinogens like UV rays and radiation, chemical carcinogens like asbestos, alcohol, smoking, and tainted food, and biological carcinogens like bacteria and viruses work as catalysts to promote unbridled cell proliferation [15–17]. There is currently no such medical treatment that can cure cancer. Therefore, early-stage detection is the best strategy to combat and reduce the mortality rate from cancer. Li et al. [18] in their literature, put forward a sensor for the early detection of breast cancer cells using an electrochemical method. Li et al. [19] suggested nanoparticle magnetic antigen sensing in order to dig out circulating tumor cells in breast cancer. Hajba et al. [20] reported a microfluidic sensor for detecting and capturing cancer cells. Later, Liu et al. [21] coined an optical sensor with the use of Raman spectroscopy for earlier identification of cancerous cells in the human body. Optical detection of specific dimeric nuclear protein (Estrogen) has been demonstrated with the use of microstructured PCF [22]. Bertucci et al. outlined a microstructured optical fiber Bragg grating optofluidic structure for investigating genomic DNA [23] and, the detection of lukemia cells was reported with the help of hollow core PCF [24]. Later in 2018, Ayyanar et al. [25] delineated a dual-core PCF sensor for cervical cancer cell detection and achieved high sensitivity of 10,925 nm/RIU for *y*-polarized wave. Ramanujam et al. [26] proposed a nanocomposite material coated PCF in order to detect cancer-affected cells in the human body. In the same year, Jabin et al. [27] reported titanium coated SPR-based cancer sensor to detect cancer cells from different body parts. Further, in 2020, blood cancer was detected efficiently with the help of a twin-core PCF refractive sensor [28].

This manuscript proposes a bottom side partially etched SPR-employed solid core PCF sensor for tracing different cancer cells. In this work, the sensitivity response of each cancer cell, such as skin cancer cell, cervical cancer cell, blood cancer cell, breast cancer cells (type-1 and type-2), and adrenal gland cancer cell, has been recorded separately. The proposed sensor follows the SPR technique that ensures the interaction of photons (optical light) with the gold-coated surface on which different cells (i.e., normal and cancerous) are to be placed. Moreover, for numerical investigation, we have taken liquid samples of healthy and cancer cells with concentrations of 30–70% and 80%, respectively. Simulation and mathematical interpretation of the propounded model have been carried out with the aid of FEM-based COMSOL Multiphysics software. Our work is mainly focused on the rapid detection of cancer cells from different body parts using an SPR-based simple detection technique. The uniqueness of our work can be justified as follows (i) the designed PCF is partially etched from the bottom side, due to which the distance between the core and gold-coated fiber surface is reduced. Hence, mode coupling becomes more vital, and sensitivity is enhanced against all cancer cells; (ii) The functionality of the proposed structure is based on an external sensing approach, due to which the fabrication feasibility of such structure is quite high.

2 Theoretical interpretation and geometrical descriptions

The frontal view of the proposed structure is shown in Fig. 1 in which a single-core transmission mode is supported by the suggested PCF. The core and cladding portions are made of silica material. The large-scale and small-scale size holes have been deliberately delineated in the substrate of the propounded structure. Two sizable air holes of diameter $D = 1.1$ μm are positioned horizontally to the solid core. The PCF's outer coating is embellished with a hexagonal lattice pattern made up of tiny air holes with a diameter (d) of 0.6 μm and a pitch distance of 1.8 μm. To ensure a satisfactory bonding of metal nanoparticles with fiber, the bottom portion of the proposed PCF has been partially etched and made completely flat. The distance of the flat fiber surface from center of the fiber core known as polishing height has been fixed at $h = 2.60$ μm. Subsequently, the flat portion of fiber has been decorated with the thin layer of an active metal gold having thickness $t_{Au} = 40$ nm.

The proposed structure somehow has the same appearance as conventional D-shaped fiber. However, the metal and biosample to be probed are attached to the bottom of the suggested structure, which takes advantage of the formation of a full core radius that is prudential for enhancing the surface plasmon resonance. Whereas, in conventional D-shaped fiber, a complete core radius formation

Table 1 Proposed cancer sensor sequential arrangement

Structure layout	Base material	Material type	Material RI ($n + j * k$)	Thickness
1st layer	PCF	Silica	[29]	–
2nd layer	Gold	Active metal	[30]	$t_{Au} = 40$ nm
3rd layer	Liquid sample	Healthy/Cancer cells	[25, 27, 33, 34]	–

Table 2 Tabulation of refractive index variation of various cancerous cells and their corresponding normal cells

Cancer classes	Cell categorization	Cell congregation	Refractive index	References
Adrenal gland cancer	PC12	Normal (30–70%)	1.381	[25, 27, 33, 34]
		Cancerous (80%)	1.395	
Blood cancer	Jurkat	Normal (30–70%)	1.376	
		Cancerous (80%)	1.39	
Breast cancer type-1	MDA-MB-231	Normal (30–70%)	1.385	
		Cancerous (80%)	1.399	
Breast cancer type-2	MCF-7	Normal (30–70%)	1.387	
		Cancerous (80%)	1.401	
Cervical cancer	HeLa	Normal (30–70%)	1.368	
		Cancerous (80%)	1.392	
Skin cancer	Basal	Normal (30–70%)	1.36	
		Cancerous (80%)	1.38	

is not possible; hence, the plasmon resonance is degraded, ultimately leading to sensitivity degradation of such PCF SPR sensors (Table 1).

2.1 Fabrication viability of the proposed PCF sensor

Since the propounded silica-based PCF model possesses a hexagonal lattice, it is worth starting the initial phase of fabrication of such a model with the standard stack and draw method [31]. In this method, different sizes of thin and thick capillaries, along with silica-made solid rods, can be combined with each other to shape a hexagonal pattern. The upper and bottom portions of the PCF have been etched to some finite extent to make flat surfaces. Later on, the bundled fiber is warped into a can and turned down into the final proposed PCF. Moreover, for the deposition of gold used in our proposed PCF, existing techniques like chemical vapor deposition and RF sputtering can be applied [32]. Hence, following the above steps, the proposed sensor can be realized with ease.

The experimental setup for the realization of propounded cancer sensor is demonstrated in Fig. 3. The setup components are a laser source, single mode fiber (SMF), sensing fiber, optical spectrum analyzer (OSA), and display device, respectively. An optical laser source is used to launch light into the core of the sensing fiber through SMF. The sensing fiber bears a flow cell that manages IN and OUT flow of the liquid sample (normal/cancer cells). For a specific cancer cell sample having Fixed RI, resonance occurs at a specific wavelength. The resonance wavelength changes when the sample's RI changes. The optical response of each liquid sample is analyzed by OSA, which can be practically visualized by the connecting display device.

Table 2 articulates the different cancer types, their corresponding normal and cancerous cells, and their refractive indices. The utmost concentration level of the cancer cell has been kept to 80% while the normal cell varied from 30 to 70%.

2.2 Mathematical formulation

Since the principal objective of the proposed SPR cancer sensor is to identify various cancer cells using the FEM technique, it is essential to pay attention to changes in light absorption during the detection of each liquid biosample. So, here, in this section, we have emphasized the formulation of the key parameters, such as the refractive index of the host material and dielectric constant of gold, that are primarily required to fulfill the objective mentioned earlier. Silica is the host material used in our proposed PCF model. The numerical justification of its refractive index is done by Sellmeier's equation given as follows [29]:

$$M_{\mathrm{Sio}_2} = \sqrt{1 + \sum_{k=1}^{k=3} \frac{V_K \lambda^2}{\lambda^2 - W_k^2}} \tag{1}$$

Here, M_{Sio_2} stands for silica RI and the values for coefficients V_K and W_K are easily detachable from [36].

The right plasmonic material must be chosen because the SPR-based detection technique relies on the generation of plasmons on a substrate. To do so, we have chosen gold as plasmonic material. The permittivity of gold is governed by Drude-Lorentz model because this model provides a more accurate description of the optical properties of metals, such as their reflectivity, transmittance,

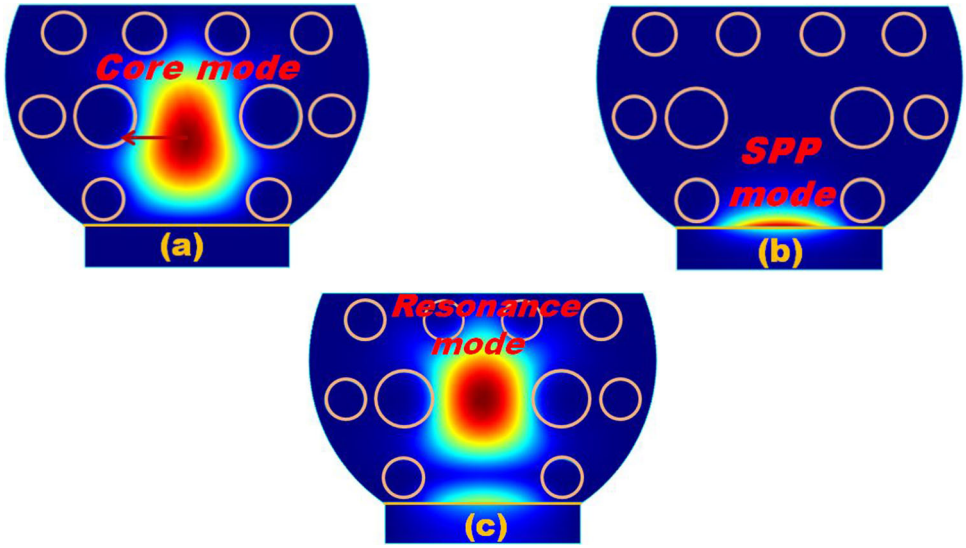

Fig. 2 Electric field confinement in **a** core guided mode, **b** SPP mode and, **c** resonance mode

and absorption, compared to the Drude model. Therefore, as per the Drude-Lorentz model, the gold permittivity is given as follows [30]:

$$\varepsilon_{\text{Gold}} = \varepsilon_{\infty} - \frac{\omega_D^2}{\omega(\omega + j\gamma_D)} - \frac{\Delta\varepsilon\Omega_L^2}{\left(\omega^2 - \Omega_L^2\right) + j\Gamma_L\omega} \tag{2}$$

Here, $\varepsilon_{\text{Gold}}$ stands for gold permittivity. ε_{∞} and $\Delta\varepsilon$ are high-frequency permittivity and weighted coefficients whose values are 5.9673 and 1.09, respectively.Γ_L and Ω_L spectrum width and oscillator strength. ω is the natural angular frequency, ω_D and γ_D are plasma and damping frequencies.

3 Result and discussion

We have kept the design of our proposed nanodevice sensor quite simple, which supports real-time sensing. The liquid biosamples that are contaminated with cancer cells can be directly placed on the bottom flat portion of the fiber rather than the sophisticated liquid sample infiltration into the chosen air cavities. The biosample that has undergone testing produces a resonant peak after being tested and confers its various operating modes. Likewise, in our work, the curve of the resonant peak for a specific cancer cell shows three modes: core mode, cancer cell mode (SPP), and resonance mode. These modes can be better visualized with the following field dispensation.

Figure 2 displays the x-polarized electric field allocation in three different modes. These modes are SPP mode, resonance mode, and core mode. It is noted that in our work, we have used biosamples as various liquid cells (healthy and cancerous). Figure 2a signifies core/normal cell mode that assures the light energy (red color) confinement within the fiber core. Figure 2b indicates first-order surface plasmon polariton (SPP) or cancer cell mode that ensures the transfer of core concentrated light to a metal–dielectric interface. Moreover, the major reason for choosing the first-order SPP mode is that it accelerates with the fundamental mode to obtain significant phase matching. Further, the SPR phenomenon can be visualized in Fig. 2c. Under this phenomenon, the energy of both core and cancer cell modes gets coupled, referred to as resonance or coupling mode, as getting this mode for each cell is necessary for successful cancer cell detection. After analyzing field distributions, further analysis of the proposed cancer sensor model in terms of its effective refractive index (real and imaginary parts) is carried out by FEM.

The bio-liquid sample (normal and cancerous) to be investigated is gently placed on a flat fiber surface called a sensing medium. Initially, the first liquid sample in the form of a Jurkat cell is picked to observe the individual coupling responses of its healthy and cancer cells, shown in Fig. 3. The electric field expansion for Jurkat's normal and cancer cells starts at a lower wavelength. Later on, when the wavelength rises, transposition of field energy is presumed between normal and cancer cell modes. At the interacting point where the values of the real fraction of effective refractive indices (RIs) of these two specific modes become equal, power is uniformly distributed to them, and hence, the maximum coupling loss in the form of a resonant peak is obtained. The wavelength at which the resonant peak appears is called resonance wavelength (λ_r) as λ_r fulfills phase-matching criteria between Jurkat's normal/cancer cell core and SPP modes.

In Fig. 3, it is noticed that the fundamental and SPP modes of Jurkat's normal cell resonate at $\lambda_r = 2150$ nm whereas the resonating wavelength for Jurkat's cancer cell fundamental and SPP modes appears at 1825 nm. Hence, the maximum resonant peak

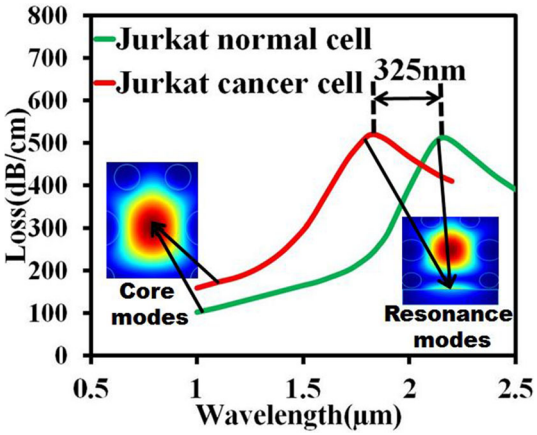

Fig. 3 Loss curve variations for Jurkat's normal (green color) and cancer (red color) cells in core mode and resonance mode

divergence for Jurkat's cancer cell with respect to its normal cell is 325 nm. Moreover, the formula for calculating peak/confinement loss (γ_{CL}) for the propounded cancer sensor during the coupling between core and SPP mode is given as follows [35]:

$$\gamma_{CL} = 8.686 * 2\pi / \lambda * \mathrm{Im}(n_{\mathrm{eff}}) * 10^4 \ \mathrm{dB/cm} \tag{3}$$

Here, $\mathrm{Im}(n_{\mathrm{eff}})$ stands for the imaginary fraction of PCF's effective refractive index and λ is the wavelength of operation.

Therefore, with the help of the above Eq. 3, the *x*-polarized peak loss values for Jurkat's cancer and normal cells are 520.66 dB/cm and 512.87 dB/cm, respectively.

It is clearly shown in Fig. 3 that λ_r for Jurkat cell shifts by 325 nm with respect to its normal cell. Further, with the help of a calculated shift in resonance wavelength ($\Delta\lambda_r$), the wavelength sensitivity can be estimated as follows [36]:

$$S_\lambda = \Delta\lambda_r / \Delta n_a \ \mathrm{nm\ RIU^{-1}} \tag{4}$$

Here, S_λ stands for wavelength sensitivity. $\Delta\lambda_r$ and Δn_a are deviations in resonant peak and liquid sample RI.

The utmost wavelength sensitivity computed using Eq. 4 is 23,214.28 nm $\mathrm{RIU^{-1}}$, which is large enough to discriminate between Jurkat's normal and cancer cells.

The figure of merit (FoM) is an important parameter for the analysis of SPR biosensors because it quantifies the sensitivity of the sensor, which is a key factor in determining the sensor's ability to detect analytes at low concentrations [37–39]. The FoM measures the change in the sensor's response per unit change in the concentration of the analyte being measured, divided by the full-width at half-maximum (FWHM) of the response curve. It can be expressed as follows [40].

$$\mathrm{FoM}\left(\mathrm{RIU^{-1}}\right) = \frac{S_\lambda}{\mathrm{FWHM}} \tag{5}$$

Using the above Eq. 5, the maximum possible FoM is obtained for breast cancer cell (type-2), which is around 20.1 $\mathrm{RIU^{-1}}$.

The confinement loss curves for different cells with their coupling peculiarities are shown in Fig. 4. Typically, the coupling response of each cell (normal and cancerous) demonstrated in Fig. 4a–f has been recorded in terms of their resonant peak. Initially, the coupling response is investigated for the Basal cell shown in Fig. 4a. It is evident from Fig. 4a that the resonance appears at 2420 nm wavelength for Basal's healthy cell ($n_s = 1.36$), whereas the resonance wavelength shifts to 2060 nm when the healthy cell is getting affected by the cancer cell ($n_s = 1.38$). Hence, the total divergence in resonance wavelength for Basal's cancer cell to its healthy cell is 360 nm, which holds the maximum possible wavelength sensitivity of 18,000 $\mathrm{nmRIU^{-1}}$. The next cell to be examined is HeLa, whose coupling characteristic is demonstrated in Fig. 4b. The resonant peak wavelength for HeLa's cancer cell ($n_s = 1.392$) deviates to 1820 nm from its healthy cell ($n_s = 1.368$) peak wavelength of 2250 nm. Hence, the overall difference in resonance wavelength between HeLa's normal and cancer cells is 430 nm which ends with a very high sensitivity of 17,916.66 $\mathrm{nmRIU^{-1}}$. Subsequently, the coupling analysis is done for the rest of the cells (Jurkat, MDA-MB-231, MCF7, and PC12) shown in Fig. 4c–f.

In Fig. 4d and e, the resonance wavelengths for healthy breast cells (type 1 and type 2) are 1840 nm and 1830 nm. But, the change in resonance wavelengths has been observed when healthy breast cells are getting affected by cancer cells. Therefore, the changed wavelengths for cancer cells type 1 and type 2 are 1570 nm and 1510 nm. Due to this, the differences in resonance wavelength are 270 nm and 320 nm, respectively. The last examined cell is PC12 (adrenal gland), in which the measured resonant peak difference between its normal and cancer cell is 250 nm, resulting in a maximum sensitivity of 17,857.14 $\mathrm{nmRIU^{-1}}$.

3.1 Influence of geometric and material parameters on sensing performance

In this section, we have discussed how mode coupling characteristics are getting affected by material and geometrical parameters such as the thickness of gold (Au) and the diameter of large and small air holes.

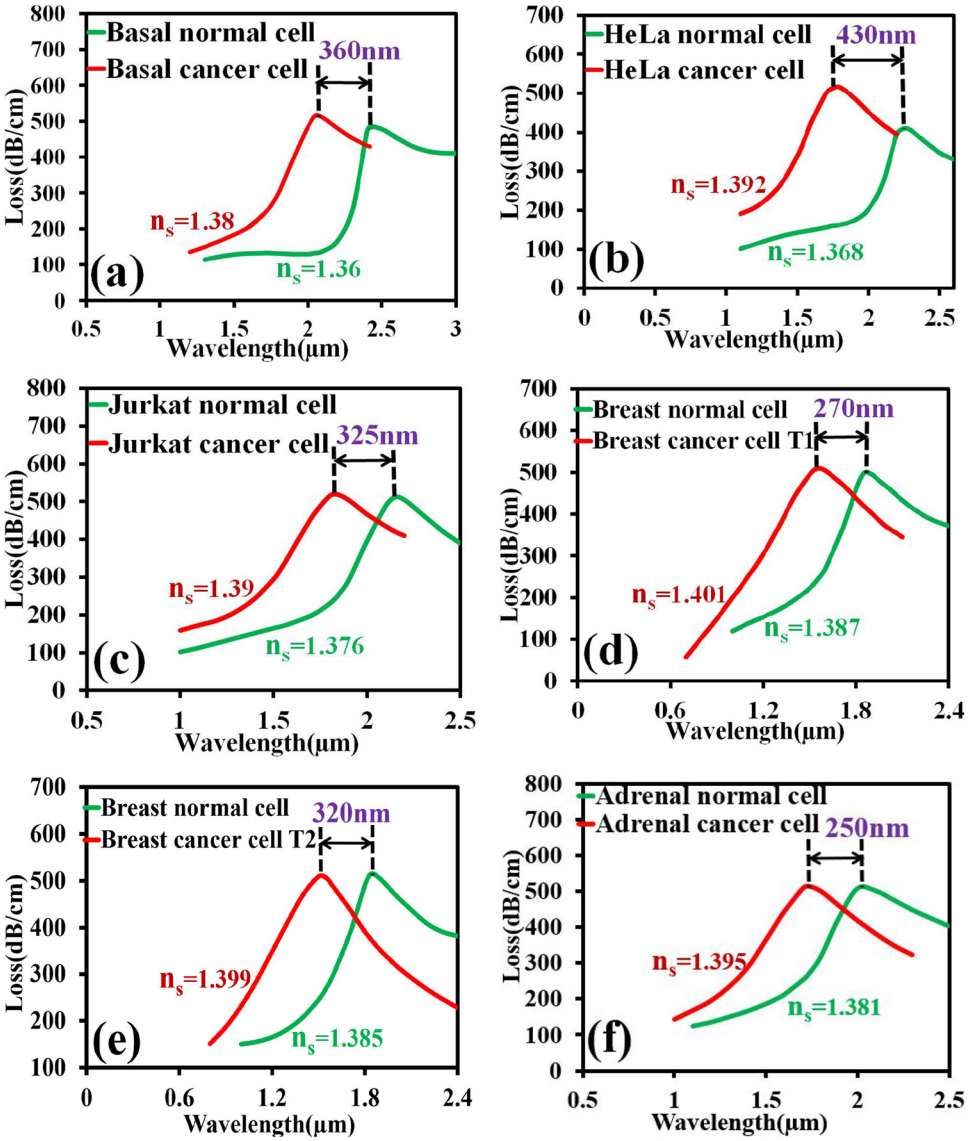

Fig. 4 Mode loss curves for cancer and normal cells of **a** Basal, **b** HeLa, **c** Jurkat, **d** Breast T-1, **e** Breast T-2 and **f** Adrenal gland

3.1.1 Influence of gold thickness on mode coupling loss

While designing an SPR-based biosensor, it is necessary to optimize the thickness of plasmonic material as it influences the resonance wavelength position as well as the depth of the resonant peak. Here, in our work, we have chosen gold as plasmonic material and investigated the sensing performance of the proposed biosensor by altering its thickness (t_{Au}). We have specifically selected one of the cells, HeLa, to demonstrate how gold thickness impacts the resonance wavelength and modal loss of the chosen cell. It is evident from Fig. 5 that the resonant peak shifts right toward a higher wavelength with gold thickness. However, the resonant peak depth decreases in the form of coupling loss.

The strongest resonance for HeLa's normal and cancer cells appeared at $t_{Au} = 40$ nm as the mode coupling losses for both the cells are highest at this thickness, i.e., 417 dB/cm and 515 dB/cm. Moreover, the modal losses for normal and cancer cells at $t_{Au} =$ 45 nm, 50 nm are 395 dB/cm, 355 dB/cm, 479 dB/cm and 432 dB/cm. Hence, our optimized gold thickness for the proposed PCF design is 40 nm. Notably, we have done the thickness analysis up to 50 nm because the further increase in t_{Au} gives rise to higher damping losses that weaken the mode coupling effectiveness.

3.1.2 Influence of small air holes and polishing height

Figure 6a–c displays variation in resonant peak against HeLa's normal and cancerous cells due to PCF's major geometrical parameters such as polishing height (h), diameter of large and small air holes. The purple-colored curve shown in Fig. 6a is dedicated to HeLa's

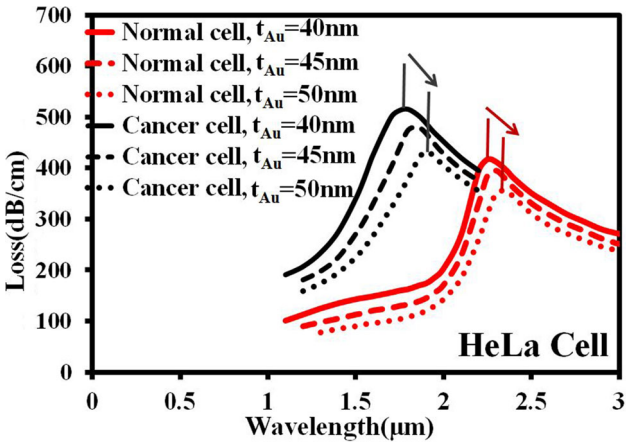

Fig. 5 Effect of varying gold thickness on resonance depth (modal loss) for HeLa cell

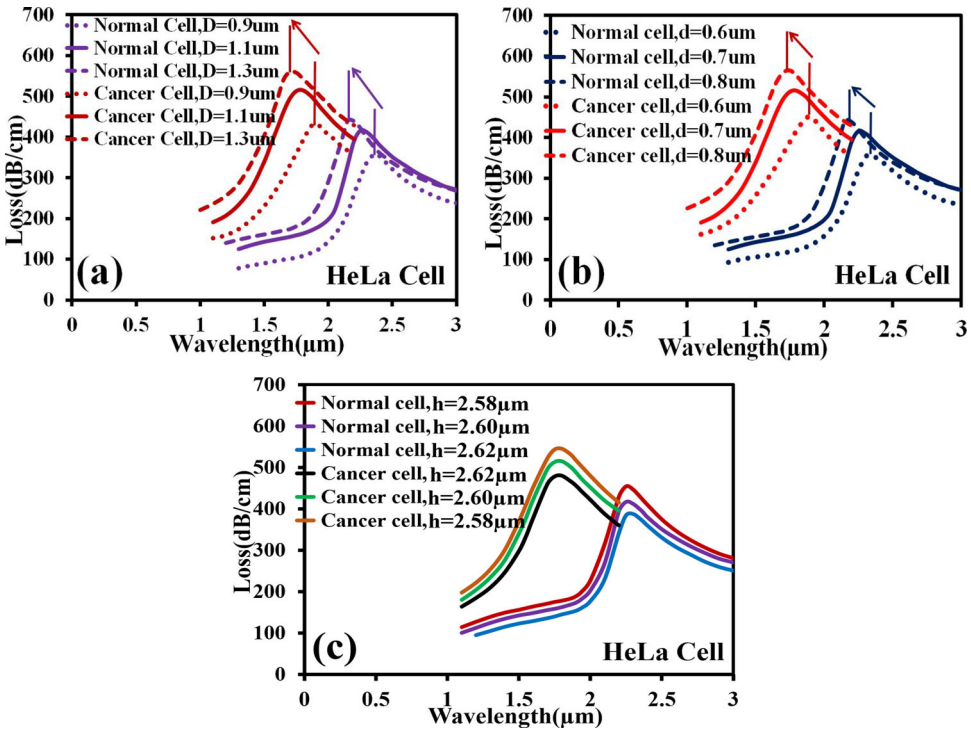

Fig. 6 Effect of varying **a** large, **b** small air hole diameter, and **c** polishing height on resonance depth of HeLa's normal and cancer cells

normal cells, while the red one is for cancer-affected cells. It is evident from Fig. 6a and b that alteration in air hole diameter mainly affects the modal loss.

As illustrated in Fig. 6a and b, when diameters of the large(D) and small(d) air holes increase from $D = 0.9$ to 1.3 μm, and $d =$ 0.6–0.8 μm, the resonance wavelength for HeLa's normal and cancer cells shift left toward lower wavelength with their increasing resonant peaks (indicated by different colored arrows) in the form of modal loss. In Fig. 6a, the highest mode loss values measured at $D = 1.3$ μm for normal and cancer cells are 439.5 dB/cm and 560 dB/cm, while the minimum loss is observed at $D = 0.9$ μm. The mode loss curve shown in Fig. 6b against small air hole diameter (d) followed a similar resonant peak trajectory as mentioned in Fig. 6a. Hence, the maximum possible mode loss values (i.e., 440 dB/cm and 565 dB/cm) for normal and cancer cells are obtained at $d = 0.8$ μm. In the end, the overall impression drawn from Fig. 6a and b is that the mode coupling loss rises when the diameter of large and small air holes increases. It is because the increase in air hole diameter squeezes the core light energy and transfers it to the dielectric-metal interface, which is essential for effective interaction between core and SPP modes. Figure 6c displays how polishing height affects modal loss. The mode coupling gets stronger with reducing polishing height. When polishing depth decreases from 2.62 to 2.58 μm, the coupling loss increases, since a reduction in polishing height provides a shorter distance between the core and the gold-coated surface, which encourages better coupling of field energy between fundamental and SPP modes. We have kept polishing height at $h = 2.6$ μm. In addition, it is important to note in Fig. 6c that the resonance peak is still there at the same wavelength despite a change in polishing depth from.

Table 3 Numerical assessment of multiple cancer cells in terms of their wavelength sensitivities

Cell group	Cell stage	RI	λ_r (nm)	$\Delta\lambda_r$ (nm)	S_λ (nm/RIU)	Detection limit
Basal	Normal	1.36	2420	360	18,000	0.02
	Cancerous	1.38	2060			
HeLa	Normal	1.368	2250	430	17,916.66	0.024
	Cancerous	1.392	1820			
Jurkat	Normal	1.376	2150	325	23,214.28	0.014
	Cancerous	1.39	1825			
MDA-MB-231	Normal	1.385	1840	270	19,285.71	0.014
	Cancerous	1.399	1570			
MCF7	Normal	1.387	1830	320	22,857.14	0.014
	Cancerous	1.401	1510			
PC12	Normal	1.381	1990	250	17,857.14	0.014
	Cancerous	1.395	1740			

Table 4 Performance-wise comparison of the proposed cancer sensor with pre-reported cancer sensors

PCF/prism designs	Cancer category	Cell category	Sensitivity (nm/RIU), (deg./RIU)	References
1-Dimensional PC	Blood cancer	Jurkat	42.5	[26]
	Cervical cancer	HeLa	42.95	
	Adrenal gland cancer	PC12	42.22	
	Breast cancer T-1	MDA-MB-231	42.85	
	Breast cancer T-2	MCF-7	43.13	
Hexagonal patterned single core PCF	Cervical	HeLa	5416.66	[25]
	Breast	MDA-MB-231	5714.28	
	Skin	Basal	4500	
Hexagonal lattice-based twin-core PCF	Blood cancer	Jurkat	8571.43	[28]
1D PC-based structure	Skin cancer	Basal	718.6	[41]
			714.3	
External sensing based circular PCF	Cervical cancer	HeLa, INBL	10,000	[42]
	Skin cancer	Basal	5000	
	Adrenal gland cancer	PC12	10,714.28	
	Blood cancer	Jurkat, JM	5416.66	
	Breast cancer T-1	MDA-MB-231	12,142.85	
	Breast cancer T-2	MCF-7	12,857.14	
Prism based structure	Blood	Jurkat	229	[43]
	Cervical	HeLa	384	
	Skin	Basal	292	
	Adrenal gland	PC12	242	
	Breast cancer T-1	MDA-MB-231	254	
	Breast cancer T-2	MCF-7	261	
Bottom side polished D-shaped PCF	Skin cancer	Basal	18,000	Proposed work
	Cervical cancer	HeLa	17,916.66	
	Blood cancer	Jurkat	23,214.28	
	Breast cancer type-1	MDA-MB-231	19,285.71	
	Breast cancer type-2	MCF-7	22,857.14	
	Adrenal gland cancer	PC12	17,857.14	

The wavelength sensitivity response of the proposed sensor for different cell groups is shown in Table 3. Each cell group, such as Basal, HeLa, Jurkat, MDA-MB-231, MCF-7, and PC12, shows distant resonant peaks for its normal and cancerous cells, and the corresponding resonant peak deviations between their healthy and cancer cells are 360 nm, 430 nm, 325 nm, 270 nm, 320 nm and 250 nm, respectively. The highest wavelength sensitivity, i.e., $S_\lambda = 23214.28$ nm/RIU is found for Jurkat cell, dedicated to blood cancer. Additionally, our proposed cancer sensor's upper detection limit is 0.024.

A brief comparison of the proposed cancer sensor with other already reported cancer sensors is made on the basis of their sensitivity performances, shown in Table 4. Apart from PCF-based biosensors, we have also compared the performance statistics of one prism-based structure [37] in the above table, whose sensitivity is measured in degree/RIU. It is found that the estimated values of sensitivity for all six different cancer cells are greater than the other recently reported cancer sensors cited in Table 4.

4 Conclusion

A D-shaped dual-side etched SPR-based biosensor has been proposed for the detection of different cancer cells. Each cancer-affected cell has been successfully detected from their respective healthy cells by differentiating their resonant peaks. SPR is achieved by depositing a plasmonic metal gold on the flat bottom surface of the proposed PCF. A total of six different cells have been investigated to calculate the relative sensitivities. These cells are Basal, HeLa, Jurkat, MDA-MB-231, MCF-7, and PC12. When their healthy and cancer-affected liquid samples are applied to the metal-coated flat surface, distinct resonant peaks are obtained for both samples due to their refractive index difference. Therefore, with the help of obtained resonant peak differences between healthy and cancer samples of all six cells, the calculated sensitivities for skin, cervical, blood, breast (T-1 and T-2), and adrenal gland cancer cells are 18,000 nm/RIU, 17,966.66 nm/RIU, 23,214.28 nm/RIU, 19,285.71 nm/RIU, 22,857.14 nm/RIU and 17,857.14 nm/RIU, respectively. Hence, our proposed biosensor is greatly suggested due to its potential to detect verities of cancer cells and due to its fabrication compatibility.

Author contributions Conceptualization: [SS], Methodology: [BC], Formal analysis and investigation: [SS and AU], Writing—original draft preparation: [SS]; Writing—review and editing: [SAT].

Funding The authors did not receive support from any organization for the submitted work.

Data availability All data generated or analyzed during this study are included in this published article.

Declarations

Competing interests The authors declare that they have no known competing financial interests or personal relationships that could have appeared to influence the work reported in this paper.

References

1. J. Broeng, D. Mogilevstev, S.E. Barkou, A. Bjarklev, Photonic crystal fibers: a new class of optical waveguides. Opt. Fiber Technol. **5**, 305–330 (1999)
2. Y. Wang, X. Zhang, X. Ren, L. Zheng, X. Liu, Y. Huang, Design and analysis of a dispersion flattened and highly nonlinear photonic crystal fiber with ultralow confinement loss. Appl. Opt. **49**, 292–297 (2010)
3. A. Upadhyay, S. Singh, D. Sharma, S.A. Taya, A highly birefringent bend-insensitive porous core PCF for endlessely single-mode operation in THz regime: an analysis with core porosity. Appl. Nanosci. **11**, 1021–1030 (2021)
4. J. Zubia, J. Arrue, Plastic optical fibers, "An introduction to their technological and applications." Opt. Fiber Technol. **7**, 101–140 (2001)
5. T.M. Monro, D.J. Richardson, N.G.R. Broderick, P.J. Bennett, Holey optical fibers: an efficient modal model. J. Lightwave Technol. **17**, 1093–1102 (1999)
6. Y. Zhao, D. Wu, R.Q. Lv, Magnetic field sensor based on photonic crystal fiber taper coated with ferrofluid. IEEE Photonic Technol. Lett. **27**, 26–29 (2015)
7. N. Nallusamy, R.V.J. Raja, G.J. Raj, Highly sensitive nonlinear temperature sensor based on modulational instability technique in liquid infiltrated photonic crystal fiber. IEEE Sens. J. **17**, 3720–3727 (2017)
8. J. Villatoro, V. Finazzi, V.P. Minkovich, V. Pruneri, G. Badenes, Temperature-insensitive photonic crystal fiber interferometer for absolute strain sensing. Appl. Phys. Lett. **91**, 091109 (2007)
9. N. Ayyanar, D. Vigneswaran, M. Sharma, M. Sumathi, M.S. Mani Rajan, S. Konar, Hydrostatic pressure sensor using high birefringence photonic crystal fibers. IEEE Sens. J. **17**(3), 650–656 (2017)
10. D. Vigneswaran, N. Ayyanar, M. Sharma, M. Sumathi, M. Rajan, K. Porsezian, Salinity sensor using photonic crystal fiber. Sens. Actuator A: Phys. **269**, 22–28 (2018)
11. W. Li, H. Cheng, M. Xia, K. Yang, An experimental study of pH optical sensor using a section of no-core fiber. Sens. Actuator A: Phys. **199**, 260–264 (2013)
12. D. Sun, T. Guo, Y. Ran, Y. Huang, B.-O. Guan, In-situ DNA hybridization detection with a reflective microfiber grating biosensor. Biosens. Bioelectron. **61**, 541–546 (2014)
13. B. Luo, Z. Yan, Z. Sun, J. Li, L. Zhang, Novel glucose sensor based on enzyme-immobilized 81° tilted fiber grating. Opt. Express **22**, 30571–30578 (2014)
14. H.H. Nguyen, J. Park, S. Kang, M. Kim, Surface plasmon resonance: a versatile technique for biosensor applications. Sensors **15**, 10481–10510 (2015)

15. J. Sasco, M.B. Secretan, K. Straif, Tobacco smoking and cancer: a brief review of recent epidemiological evidence. Lung Cancer **45**, S3–S9 (2004)
16. P. Anand, A.B. Kunnumakkara, C. Sundaram, K.B. Harikumar, S.T. Tharakan, O.S. Lai, B. Sung, B.B. Aggarwal, Cancer is a preventable disease that requires major lifestyle changes. Pharm. Res. **25**, 2097–2116 (2008)
17. C. De Martel, J. Ferlay, S. Franceschi, J. Vignat, F. Bray, D. Forman, M. Plummer, Global burden of cancers attributable to infections in 2008: a review and synthetic analysis. Lancet Oncol. **13**, 607–615 (2012)
18. T. Li, Q. Fan, T. Liu, X. Zhu, J. Zhao, G. Li, Detection of breast cancer cells specially and accurately by an electrochemical method. Biosens. Bioelectron. **25**, 2686–2689 (2010)
19. F.R. Li, Q. Li, H.X. Zhou, H. Qi, C.Y. Deng, Detection of circulating tumor cells in breast cancer with a refined immunomagnetic nanoparticle enriched assay and nested-RT-PCR. Nanomed. Nanotechnol. **9**, 1106–1113 (2013)
20. L. Hajba, A. Guttman, Circulating tumor-cell detection and capture using microfluidic devices. TrAC Trends Anal. Chem. **59**, 9–16 (2014)
21. S. Liu, L. Li, Z. Chen, N. Chen, Z. Dai, J. Huang, B. Lu, Surface-enhanced Raman spectroscopy measurement of cancerous cells with optical fiber sensor. Chin. Opt. Lett. **12**, 13001 (2014)
22. P. Saraswathi, V.K. Shinoj, M.V. Matham, P. Padmanabhan, Highly sensitive optical detection of specific protein in breast cancer cells using microstructured fiber in extremely low sample volume. J. Biomed. Opt. **15**, 017005 (2010)
23. A. Bertucci, A. Manicardi, A. Candiani, S. Giannetti, A. Cucinotta, G. Spoto, M. Konstantaki, S. Pissadakis, S. Selleri, R. Corradini, Detection of unamplified genomic DNA by a PNA based microstructured optical fiber (MOF) Bragg-grating optofluidic system. Biosens. Bioelectron. **63**, 248–254 (2015)
24. A. Khetani, A. Momenpour, E.I. Alarcon, H. Anis, Hollow core photonic crystal fiber for monitoring leukemia cells using surface enhanced Raman scattering (SERS). Biomed. Opt. Express **6**, 4599–4609 (2015)
25. N. Ayyanar, G.T. Raja, M. Sharma, D.S. Kumar, Photonic crystal fiber-based refractive index sensor for early detection of cancer. IEEE Sens. J. **18**, 7093–7099 (2018)
26. N.R. Ramanujam, I. Amiri, S.A. Taya, S. Olyaee, R. Udaiyakumar, A.P. Pandian, Enhanced sensitivity of cancer cell using one dimensional nano composite material coated photonic crystal. Microsyst. Technol. **25**, 189–196 (2019)
27. M.A. Jabin, K. Ahmed, M.J. Rana, B.K. Paul, M. Islam, D. Vigneswaran, Surface plasmon resonance based titanium coated biosensor for cancer cell detection. IEEE Photon. J. **11**, 3700110 (2019)
28. M.A. Mollah, M. Yousufali, I.M. Ankan, M.M. Rahman, H. Sarker, K. Chakrabarti, Twin core photonic crystal fiber refractive index sensor for early detection of blood cancer. Sens. Bio-Sens. Res. **29**, 100344 (2020)
29. S.K. Pandey, S. Singh, Y.K. Prajapati, A novel PCF design with an ultra-flattened dispersion and low confinement loss by varying tiny air-hole concentration at core and cladding. Opt. Rev. **28**, 304–313 (2021)
30. S. Singh, Y.K. Prajapati, Antimonene-gold based twin-core SPR sensor with a side-polished semi-arc groove dual sensing channel: an investigation with 2D material. Opt. Quantum Electron. **54**, 1–14 (2022)
31. R. Zakaria, W. Kam, Y.S. Ong, S.F.A.Z. Yusoff, H. Ahmad, W.S. Mohammed, Fabrication and simulation studies on D-shaped optical fiber sensor via surface plasmon resonance. J. Mod. Opt. **64**(14), 1443–1449 (2017)
32. G. An, S. Li, W. Qin, W. Zhang, Z. Fan, Y. Bao, High-sensitivity refractive index sensor based on D-shaped photonic crystal fiber with rectangular lattice and nanoscale gold film. Plasmonics **9**, 1355–1360 (2014)
33. G.P. Mishra, D. Kumar, V.S. Chaudhary, G. Murmu, Cancer cell detection by a heart-shaped dual-core photonic crystal fiber sensor. Appl. Opt. **59**, 10321–10329 (2020)
34. M.M.A. Eid, A.N.Z. Rashed, A.A.M. Bulbul et al., Mono-rectangular core photonic crystal fiber (MRC-PCF) for skin and blood cancer detection. Plasmonics **16**, 717–727 (2021)
35. S. Singh, A. Upadhyay, D. Sharma, S.A. Taya, A comprehensive study of large negative dispersion and highly nonlinear perforated core PCF: theoretical insight". Phys. Scr. **97**, 065504 (2022)
36. S.K. Patel, J. Parmar, H. Trivedi, R. Zakaria, T.K. Nguyen, V. Dhasarathan, Highly sensitive graphene-based refractive index biosensor using gold metasurface array. IEEE Photonics Technol. Lett. **32**, 681–684 (2020)
37. S. Khani, M. Hayati, Optical sensing in single-mode filters base on surface plasmon H-shaped cavities. Optics Communications **505**, 127534 (2022)
38. S.N. Khonina, N.L. Kazanskiy, M.A. Butt, A. Kaźmierczak, R. Piramidowicz, Plasmonic sensor based on metal-insulator-metal waveguide square ring cavity filled with functional material for the detection of CO_2 gas. Opt. Express **29**, 16584–16594 (2021)
39. S. Khani, M. Afsahi, Optical refractive index sensors based on plasmon-induced transparency phenomenon in a plasmonic waveguide coupled to stub and nano-disk resonators. Plasmonics **18**, 255–270 (2023)
40. N.L. Kazanskiy, S.N. Khonina, M.A. Butt, A. Kaźmierczak, R. Piramidowicz, A numerical investigation of a plasmonic sensor based on a metal-insulator-metal waveguide for simultaneous detection of biological analytes and ambient temperature. Nanomaterials **11**, 2551 (2021)
41. S. Khani, M. Hayati, Optical biosensors using plasmonic and photonic crystal band-gap structures for the detection of basal cell cancer. Sci. Rep. **12**, 5246 (2022)
42. A. Ramola, A. Marwaha, S. Singh, Design and investigation of a dedicated PCF SPR biosensor for CANCER exposure employing external sensing. Appl. Phys. A **127**, 643 (2021)
43. A. Uniyal, B. Chauhan, A. Pal, Y. Singh, Surface plasmon biosensor based on Bi_2Te_3 antimonene heterostructure for the detection of cancer cells. Appl. Opt. **61**, 3711–3719 (2022)